RESEARCH ARTICLE

Yan Lavallée · Shanaka L. de Silva · Guido Salas ·
Jeffrey M. Byrnes

Explosive volcanism (VEI 6) without caldera formation: insight from Huaynaputina volcano, southern Peru

Abstract Through examination of the vent region of Volcán Huaynaputina, Peru, we address why some major explosive eruptions do not produce an equivalent caldera at the eruption site. Here, in 1600, more than 11 km^3 DRE (VEI 6) were erupted in three stages without developing a volumetrically equivalent caldera. Fieldwork and analysis of aerial photographs reveal evidence for cryptic collapse in the form of two small subsidence structures. The first is a small non-coherent collapse that is superimposed on a cored-out vent. This structure is delimited by a partial ring of steep faults estimated at 0.85 by 0.95 km. Collapse was non-coherent with an inwardly tilted terrace in the north and a southern sector broken up along a pre-existing local fault. Displacement was variable along this fault, but subsidence of approximately 70 m was found and caused the formation of restricted extensional gashes in the periphery. The second subsidence structure developed at the margin of a dome; the structure has a diameter of 0.56 km and crosscuts the non-coherent collapse structure. Subsidence of the dome occurred along a series of up to seven concentric listric faults that together accommodate approximately 14 m of subsidence. Both subsidence structures total 0.043 km^3 in volume, and are much smaller than the 11 km^3 of erupted magma. Crosscutting relationships show that subsidence occurred during stages II and III when ~2 km^3 was erupted and not during the main plinian eruption of stage I (8.8 km^3).

The mismatch in erupted volume vs. subsidence volume is the result of a complex plumbing system. The stage I magma that constitutes the bulk of the erupted volume is thought to originate from a ~20-km-deep regional reservoir based on petrological constraints supported by seismic data. The underpressure resulting from the extraction of a relatively small fraction of magma from the deep reservoir was not sufficient enough to trigger collapse at the surface, but the eruption left a 0.56-km diameter cored-out vent in which a dome was emplaced at the end of stage II. Petrologic evidence suggests that the stage I magma interacted with and remobilized a shallow crystal mush (~4–6 km) that erupted during stage II and III. As the crystal mush erupted from the shallow reservoir, depressurization led to incremental subsidence of the non-coherent collapse structure. As the stage III eruption waned, local pressure release caused subsidence of the dome. Our findings highlight the importance of a connected magma reservoir, the complexity of the plumbing system, and the pattern of underpressure in controlling the nature of collapse during explosive eruptions. Huaynaputina shows that some major explosive eruptions are not always associated with caldera collapse.

Keywords Caldera · Non-coherent collapse structure · Summit pit crater · Lava dome subsidence · Magma pressure change · Pre-existing fault · Huaynaputina volcano · Southern Peru

S. L. de Silva
Department of Space Studies, University of North Dakota,
4149 Campus Road, Grand Forks, ND 58202, USA

G. Salas
Escuela de Ingeniería Geofisica, Universidad Nacional de San Agustin,
Av. Independencia s/n, Edificio Antiguo 3er Piso, Arequipa, Peru

J. M. Byrnes
Department of Geology and Planetary Science, University of Pittsburgh,
4107 O'Hara Street, 200 SRCC, Pittsburgh, PA 15260, USA

Y. Lavallée (✉)
Department für Geo- und Umweltwissenschaften,
Ludwig-Maximilians Universität,
Theresienstrasse 41/III,
80333 München, Germany
e-mail: lavallee@min.uni-muenchen.de
Tel.: +49-89-21804221

Introduction

A canon of volcanology is that a caldera develops during large explosive eruptions, draining a magma reservoir

and forming a void in which the chamber roof collapses (Fouqué 1879; Williams 1941; Smith and Bailey 1968; Walker 1984; Lipman 1984; Druitt and Sparks 1984; Scandone 1990; Branney 1995; Moore and Kokelaar 1998). Although it is recognized that the nature and style of caldera collapse are highly variable, the association of a caldera with a major eruption is used as a primary criterion in our assessment of volcanic history and hazard at potentially active volcanoes. In older or rapidly eroded locations, the longevity of a telltale tephra deposit is considerably less than the active lifetime of a volcano, and thus the longer-lasting evidence of a caldera collapse is often the only evidence of an explosive eruption. However, relying on this criterion may be problematic since recent studies on several large-volume eruptions show no major caldera subsidence at the eruption site. These include the 20,000-b.p. eruption of Lascar in Chile (Gardeweg et al. 1998), the 1600 eruption of Huaynaputina in Peru (Adams et al. 2001; Thouret et al. 2002), the 1902 eruption of Santa Maria in Guatemala (Williams and Self 1983), the 1912 eruption of Novarupta in Alaska (Fenner 1921; Wallman et al. 1990; Hildreth and Fierstein 2000), the 1932 eruption of Quizapu in Chile (Hildreth and Drake 1992), and the 1991 eruption of Cerro Hudson in Chile (Scasso et al. 1994). These cases emphasize that the association of caldera collapse and large explosive eruptions is not universal and requires that we have a better understanding of why caldera collapse is cryptic or non-existent in some major explosive eruptions.

Since all major silicic explosive eruptions produce characteristic deposits with a general family resemblance (plinian fall, pyroclastic flow deposits, co-ignimbrite, co-plinian ash, etc), it is clear that eruption-related variables are broadly consistent across the scales of these eruptions. The different styles of caldera collapse are attributed largely to architectural variables of the volcanic system such as the geometry, size, and depth of the magma reservoir, the nature of the eruptive site, and the local and regional stress regime (Williams and McBirney 1979; Walker 1984; Lipman 1984; Branney and Kokelaar 1994; Moore and Kokelaar 1998; Acocella et al. 2000; Roche et al. 2000; Walter and Troll 2001; Lavallée et al. 2004, Kennedy et al. 2004; Folch and Marti 2004). The clues to the relative importance of these factors are most likely contained in the structural features of the caldera floor and vent region, but these are often obscured by eruptive deposits or mass wasting. A rare and valuable example for which the proximal vents and structures are preserved and exposed is Volcán Huaynaputina in southern Peru (16°36′, 70°51′; Fig. 1).

One of the largest eruptions in recorded history occurred in 1600 at Huaynaputina where at least 8 km³ of magma (dense rock equivalent, DRE) were explosively erupted in a 20–26-h period (Adams et al. 2001). A further 2 km³ of magma were sporadically erupted over the subsequent 13 days. Despite this substantial magma evacuation, a volumetrically equivalent caldera is not recognized. Herein, detailed field observations are coupled with the examination of aerial photographs and satellite images in order to understand the evolution of the vent region at Huaynaputina. In particular, observations from the vent region and the surrounding structures were conducted to constrain the character of the upper crust in which the volcano was built. We discuss the implications of structures, magma reservoir geometries, and volume of magma erupted to determine the morphologic evolution of Huaynaputina, and further our understanding of caldera formation and crustal adjustment during magmatic pressure variations. Our study shows that the main plinian eruption cored out a large vent which was subsequently filled in by a lava dome. The vent area then subsided in later eruptive stages during the formation of a small non-coherent collapse structure. In the waning stages of the eruption, dome subsidence in response to local pressure decrease in the dome led to further modification of the vent region. We use the observations at Huaynaputina in tandem with those from sites of other major explosive eruptions without collapse to address the question of why collapse can be cryptic to non-existent. In aggregate, these studies implicate the complex nature of the plumbing system (i.e., size, geometry, depth, and connectivity of the magma reservoirs) as the key factor leading to the cryptic nature of the caldera collapse at sites of some major explosive eruptions.

Geological setting

Huaynaputina volcano is part of a an active silicic volcanic field, herein referred to as the Ubinas-Huaynaputina-Ticsani system (UHTS) and inferred to measure approximately 40 by 60 km based on the distribution of eruptive centers with related bulk chemistries and isotopic signatures (Fig. 1; Adams et al. 2001; Schubring 2001; Lavallée 2003). Located 25–50 km behind and oblique to the main arc of the Central Volcanic Zone of the Andes, the volcanoes of the UHTS are positioned at the margin of the Rio Tambo graben which trends N–S (Fig. 1; Lavallée et al. in prep). The UHTS was emplaced within an extensively faulted basement hosting four fault systems, namely: N–S, NE–SW, E–W, and NW–SE. While the former two systems are associated with the Rio Tambo graben, the third system is minor and the last one consists of a series of sinistral, en echelon strike slip faults which are parallel to the Central Volcanic Zone (Lavallée et al. unpublished). A study of fault kinematics by Mercier et al. (1992) suggested that the mid-Pleistocene to present-day tectonic regime of the High Andes is characterized by a vertical maximum stress induced by the high elevation (>4,000 m), a secondary E–W compression caused by collision of the Pacific and South America plates, and a resulting N–S extension in the direction of σ3 (Fig. 1).

The temporally and spatially related deposits of the UHTS have previously been referred to as part of the Quaternary Ubinas volcanics (Mendívil 1963; James et al. 1976). Huaynaputina volcano was emplaced within the old, fluvioglacially modified amphitheatre of an ancestral extinct composite volcano (de Silva and Francis 1990; Adams et al. 2001). This ancestral volcano consists of 500 m of andesite porphyry of the Pastillo volcanic complex (James

Fig. 1 Satellite image showing the volcanoes in southern Peru (**a**), position of Huaynaputina in the UHTS (*box*), and the UHTS in South America (*inset*). The trend of the Central Volcanic Zone is sketched as *dotted lines*. (**b**) Sketch of faults and fractures present in the crust of the UHTS (modified from Lavallée, 2003). The current stress vectors of the High Andes are indicated in the *inset* (Mercier et al. 1992). The location of earthquakes that occurred in the area since 1471 are indicated by a *circle*, which includes the depth estimate (Ceresis, 1985). The volcanoes were abbreviated as such: *C:* Chachani; *M:* El Misti; *P:* Pichu Pichu; *U:* Ubinas; *Hp:* Huaynaputina; *CV:* Cerro el Volcán; *Ti:* Ticsani; *Tu:* Tutupaca; *Y:* Yukumane. The satellite image from the Shuttle Radar Topographic Mission is a courtesy of the U.S Geological Survey
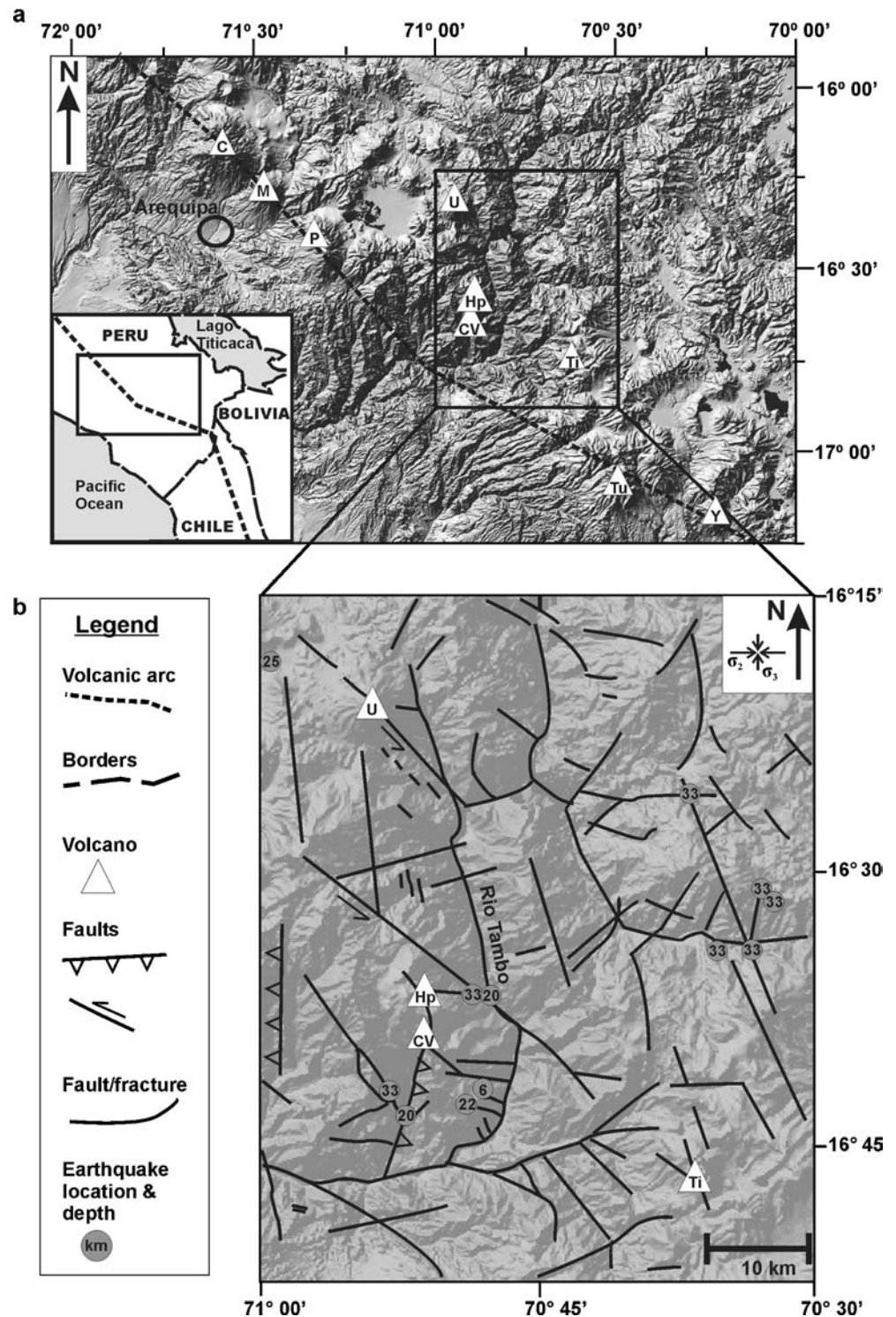
et al. 1976; Tosdal et al. 1981; INGEMMET 2000a). The Pastillo volcanics overlie Late Miocene deposits from the Capillune, Llallahui and Sencca Formations, which together comprise an additional 300–500 m of andesitic porphyry and rhyodacitic ignimbrites (Mendívil 1963; Tosdal et al. 1981).

Beneath these Cenozoic volcanics lies the Matalaque Formation, a series of Mid to Upper Cretaceous lava flows, volcanic breccias, and ignimbrites varying in composition from andesite to dacite (INGEMMET 2000a, 2000b; Carrasco Viza 2002). Deposits from the Matalaque Formation were recently recognized to crop out in the Rio Tambo graben (INGEMMET 2000a, 2000b). The graben structure protected the deposits from extensive erosion. The Matalaque Formation is more than 2 km thick and discordantly overlies the Yura Group.

Located at a depth of 3 km, the Yura Group is a series of relatively autochthonous formations of coastal sedimentary rocks deposited during the Jurassic and overthrust in the Early Late Cretaceous (Vicente 1989). The presence of the Yura Group beneath Huaynaputina also has importance herein because it has been highly fractured and faulted during overthrusting. An increase in the degree of fracturing would facilitate subsidence. Abundant Yura lithics were observed in the deposits of the 1600 Huaynaputina eruption, and their presence helps constrain the level of fragmentation in the subsurface. Beneath the Yura Formation, voluminous granodioritic gneiss from the Paleoproterozoic has been mapped as the basement of this heterogeneous stratigraphy (INGEMMET 2000a).

Previous analysis of the 1600 A.D. eruption

The historical accounts (de Silva et al. 2000), the physical volcanology (Adams et al. 2001; Thouret et al. 2002), and the petrology (Schubring 2001) of the 1600 eruption at Huaynaputina has been examined in recent studies. The eruption produced four small vents and one lava dome which are serendipitously distributed in and around the pre-existing amphitheatre (Adams et al. 2001). Variations in the stratigraphy of proximal and distal deposits require that the eruption proceeded in three stages (Fig. 2, Table 1; Adams et al. 2001). The first explosive stage erupted about 8.8 km^3 (DRE) from a NW–SE fracture, producing a 34–
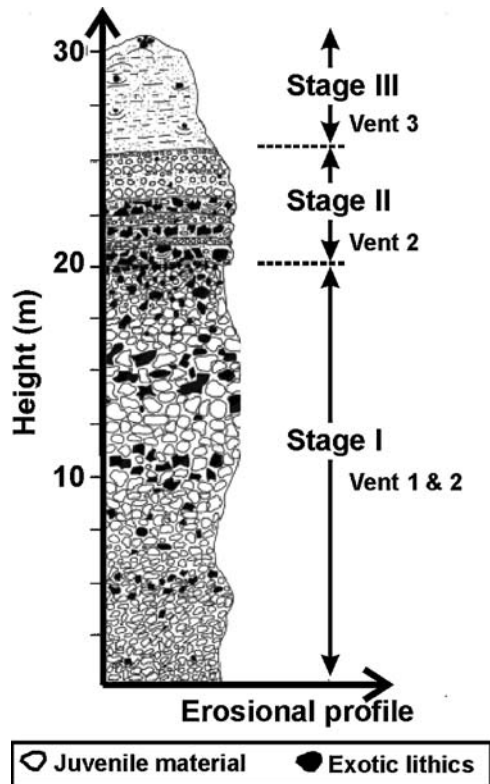
Fig. 2 Proximal stratigraphic section showing the erosional profile of the eruptive deposits of the three stages and their associated vents (modified from Adams et al. 2001)

46-km-high plinian column that extended and dispersed westward (Adams et al. 2001). A gradual intensification towards the middle of the eruption was identified which was attributed to vent enlargement through coring out of an old hydrothermal system present within the Yura Formation. This is revealed by the presence of exotic lithics in the tephra deposits of stage I (Adams et al. 2001). The upper deposits of stage I show a decrease in intensity and a dominance of andesitic lithics of the Matalaque Formation. Adams et al. (2001) estimated the volume of lithics in stage I deposits at a minimum of ~0.18 km^3.

During stage II, ~1 km^3 (DRE) was emplaced as intermittent pyroclastic flows and falls that were deposited by unstable columns probably related to intermittent choking and clearing of vent 2 (Adams et al. 2001). Stage II terminated with the extrusion of a dacitic lava dome within vent 2.

The final stage III vulcanian activity resulted in partial evisceration of the dome emplaced at the end of stage II and the formation of vent 3. Approximately 1 km^3 of coarse ash, lapilli and bombs of crystal-rich dacite were erupted and the termination of stage III was accompanied by minor subsidence along extensional faults concentric to the stage III vent (Adams et al. 2001). A late minor explosion then produced vent 4, located about 2 km south of the main eruptive site.

The petrological and geochemical character varied through the three stages (Table 1, Schubring 2001; Adams et al. 2001). Petrological analysis done by Schubring (2001) revealed the presence of two magma stability fields: one deep (>15–25 km), the other shallow (~4–6 km). To explain the early eruption of a hot, volatile-rich, crystal-poor magma followed by eruption of a cooler, volatile- and crystal-rich magma of similar composition, Schubring (2001) envisages a model where the stage I magma ascended from a deep reservoir through a shallow reservoir of crystal mush. Partial mixing of magma with the crystal mush resulted in the bimodal character of some stage II juvenile blocks and the late stage II lava dome that plugged the vent. Continued residual volatile exsolution and entrapment beneath the "plug" resulted in the intermittent vulcanian activity that defines stage III. The new work presented herein assesses the structural evolution associated with the 1600 eruption of Huaynaputina.

Methodology

The vent area was investigated in situ and through the analysis of aerial photographs (H-125–21751 to 21753; H-126–11582 to 11584; H-122–12278 to 12279 Instituto Geografico Militar, 1955, Lima Peru) and satellite images (Landsat TM, ETM, ETM+ and SRTM 90m Digital Elevation Models). These provide a clear view of the entire vent area and help identify the main lineaments. Once in the field, crosscutting relationships were identified which were used to constrain the temporal evolution of the vent structures. This was followed by an examination of faults, fractures and lineaments, which highlights the interplay between crustal structures and volcanic features.

Table 1 Description of the 1600 A.D. eruption of Huaynaputina as recorded in historical accounts (adapted from de Silva et al. 2000; Adams et al. 2001); physical parameters of the eruption (reconciled by Adams et al. 2001; Schubring 2001)

Date	Local time	Event	Eruptive stages	Physical parameters of the eruption
February 15th		Initiation of regular earthquakes		
February 18th	9:00–10:00	Occurrence of strong earthquakes felt regionally		
February 19th	11:00—13:00	Two major earthquakes of intensity 11 on the Mercalli scale		
	17:00	Nearly continuous tremors		Plinian eruption
	18:00	The whole region was dark; dry lightning and explosions were common		Mass discharge rate: 2.4×10^8 kg/s
February 20th		Major ashfall, explosions and earthquakes	Stage I	Column height: 34–46 km
	14:00	Arequipa was as dark as the night		SiO_2 content in the glass: 73%
		20–25 cm of ash accumulated in Arequipa		Magma water content: ~5%
		Intermittent roars, explosions, and earthquakes		Crystal content: 1–20%
				Magma temperature: 839 °C
				Volume erupted (DRE): ~8.8 km^3
February 21st		Clear day and little ashfall		
February 22nd		Renewed ashfall		Ashfall and pyroclastic flows
February 23rd		Quiescence		SiO_2 content in the glass: 76%
February 24th		Renewal of ashfall and intense earthquakes	Stage II	Water content: ~4%
February 25th		Very cloudy and dark, minimal ashfall		Crystal content: 25–30%
February 26th		Renewal of ashfall		Magma temperature: 773 °C
				Volume erupted (DRE): ~1 km^3
February 27th		Quiescence	Dome growth	
February 28th		Large earthquake felt in Arequipa, then renewal of ash fallout		Vulcanian activity
				SiO_2 content in the glass: 76%
March 1st		Big earthquakes and ashfall continued	Stage III	Water content: ~4%
				Crystal content: 27–40%
March 6th		Cessation of ashfall		Magma temperature: 777 °C
				Volume erupted (DRE): ~1 km^3
April 2nd		Atmosphere finally cleared		

The trends and dipping angles of faults were measured with a Brunton compass. The fault displacements were calculated by using the values of dip angles and apparent displacements measured with a measuring tape along the fault planes. Larger distances were scaled on the aerial photograph via the horizontal extent of features measured in the field. The volumes of the structures were then estimated while combining the length and angles measured with trigonometrical equations for geometrical shapes.

Observations

Examination of the vents of Huaynaputina, their alignment, and features in and around the amphitheatre provides a detailed reconstruction of the vent evolution. The influence of the NW–SE fracture at Huaynaputina is seen in its control of the pre- 1600 A.D. emplacement of a dome and a dike within the northern and southern walls of the amphitheatre, respectively (Fig. 3). Vents 1 and 3 are located along the fracture as well, and the dike feeding the central dome emplaced at the end of stage II is exposed within those vents (Fig. 4). The vents are also positioned at its intersection with an E–W trending fault (F_1) that parallels the collapse direction of the ancestral amphitheatre (Fig. 5). F_1 further reveals subsidence within vent 2.

The walls and floor of vent 2 show variable elevations and are offset by two E–W faults, F_1 and F_2 (Fig. 3). F_1 is defined by a bench crossing vent 3 and extends westward as a zone of slumped loose debris in the wall of the amphitheatre, and extends eastward into the wall of vent 2 while offsetting the central sector from the southern sector

Fig. 3 Aerial photograph (portion of H-125-217520 Instituto Geografico Militar, Lima, Peru 1955) of the ancestral amphitheatre housing the four vents of Huaynaputina, as identified by Adams and et al. (2001). The pre-1600 dome and dike are also indicated in the northeastern and southern walls of the amphitheatre. Proximal structures shown. The *contour lines* indicate the four subsidence faults: F_1, F_2, F_3, F_4, and the peripheral gashes (*E*). The inferred western side of F_3 is shown by a *dotted line*, and the NW–SE fractures are shown by the *dashed lines*
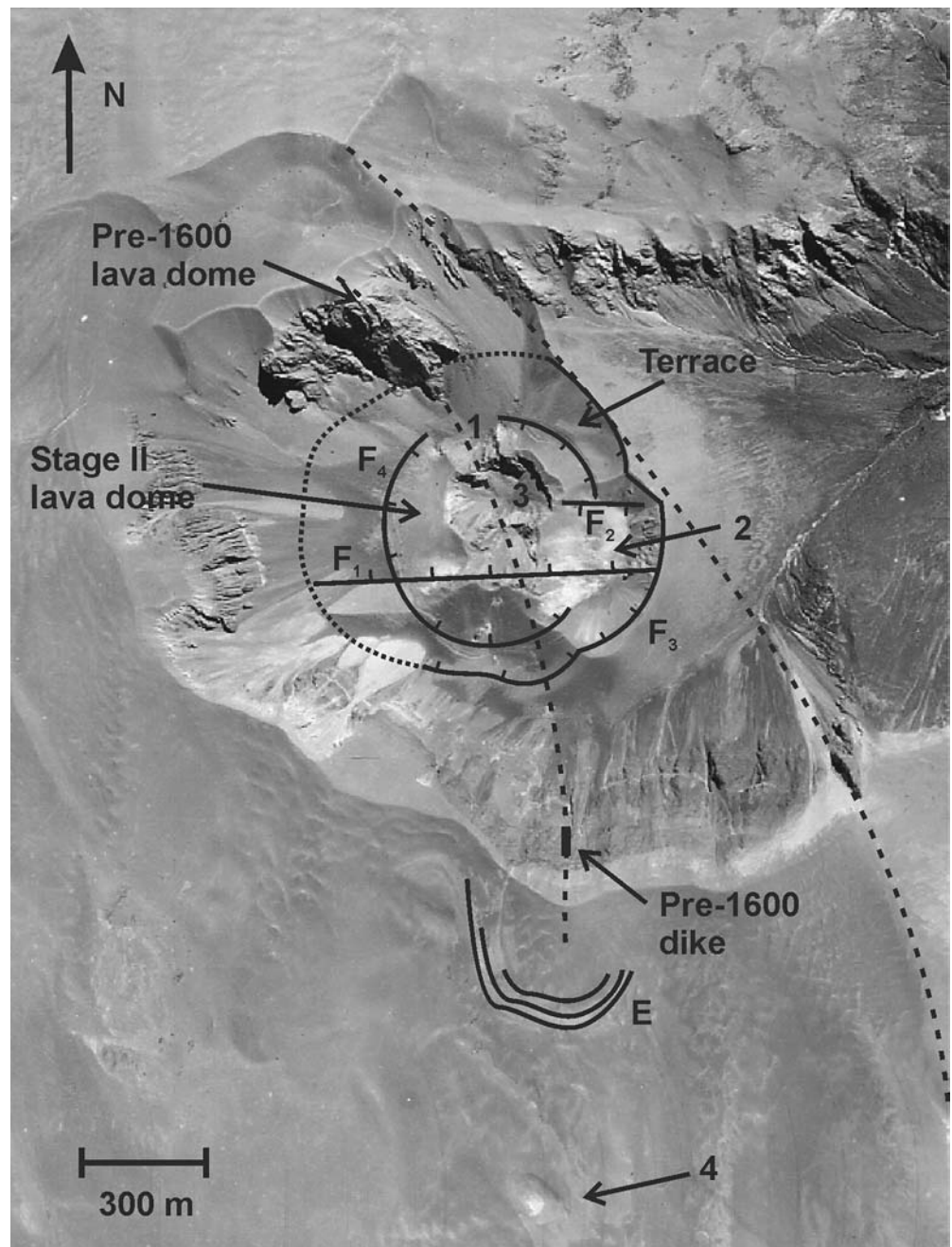
by approximately 50 m (Fig. 5). At the base of the F_1 fault scarp, two small ~50-m-wide depressions are aligned E–W (Fig. 5a). The dip of F_1 was difficult to estimate due to slumping of debris that eroded the fault plane, but the trace of F_1 is manifested in the eastern wall of vent 2 where a vertical dike was emplaced. The associated fault, F_2, divides the central sector of vent 2 from the northern sector by a variable displacement of 20–70 m (Fig. 4a). The displacement is variable because the northern sector is a terrace that is tilted toward the center of vent 2 by ~25°, assuming an initially horizontal surface (Fig. 4a). Interestingly, F_1 and F_2 are only slightly buried, which indicates that little tephra was erupted and deposited after the subsidence.

Subsidence at F_1 and F_2 occurred in combination with a third fault (F_3) which had previously been referred to by Adams et al. (2001) as the wall of vent 2 (Fig. 3 and 5).

The eastern wall of vent 2 is made of crystal-rich dacite containing orthopyroxene unlike the orthopyroxene-free dacite that built the stage II lava dome (Adams et al. 2001); the former dacite is the remnant of a pre-1600 dome that once partly covered the amphitheatre. Subsequent subsidence of the hanging block along F_3 enlarged and lowered the vent area (Fig. 3 and 5). Displacement is variable around F_3; in the eastern sector, F_3 has more than 70 m of subsidence, while the northeast and southern sectors show approximately 3 and 20 m, respectively. The fault plane,
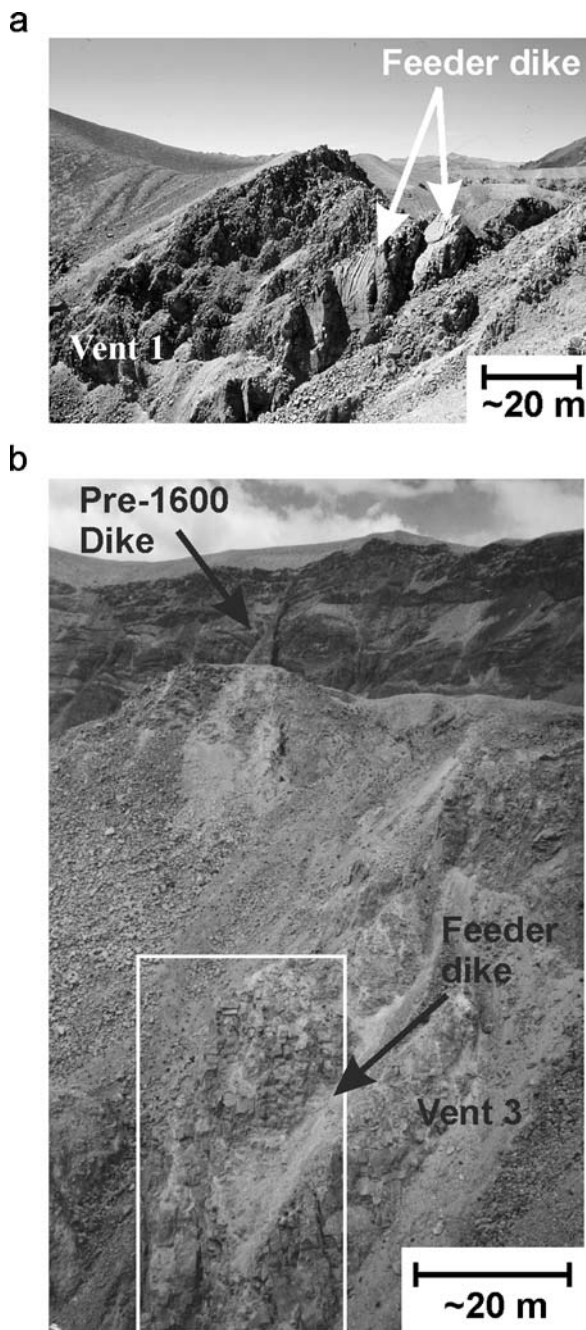
Fig. 4 Photographs of features illustrating the presence of a dike emplaced within the NW–SE fracture. (**a**) Photo of the dike in vent 1 (looking W); (**b**) photo of the dike in vent 3 and the pre-1600 dike in the wall of the amphitheatre, seen in the background (looking S)

partially buried in the last two sectors, is best exposed in the eastern sectors with the E–W dike in the wall of vent 2 faulted by F_3 at a dip angle exceeding 75° (Fig. 5c). In the western sector, abundant slumping of unconsolidated tephra from the amphitheatre wall masks the presence of F_3, which can only be inferred (dotted line F_3; Fig. 3). The dimensions of F_3, and thus the first subsidence structure were estimated at approximately 0.85 by 0.95 km. Examination of aerial photographs suggests that there may have been broader subsidence (Fig. 3). Midway between the

southern amphitheatre rim and vent 4, the NW–SE fracture intersects the N–S fault that extends from Quebrada Volcán and Cerro el Volcán. At this intersection, which is approximately 1.5 km south of vent 3, a series of three to four unburied arcuate extensional gashes which curve toward the vent area can be distinguished (E on Fig. 3). Their traces extend over approximately 0.6 km. Also, another NW–SE lineation which bounds Huaynaputina to the east can be identified (Fig. 3). Within the vent area, the lineation coincides with the northeastern segment of F_3 that borders the tilted terrace.

A second subsidence structure was identified which is defined by a set of concentric extensional faults (F_4) peripheral to vent 3 (Fig. 3 and 5a). The well-preserved faults crosscut F_1, F_2 and the stage III tephra; they were neither buried nor eroded (Fig. 3 and 6). The F_4 feature defines a structure with a diameter of nearly 0.56 km and depending on the location, the number of faults constituting F_4 varies between two and seven. Measurements of dip angle show an outward steepening progression. Approximately 35 m of displacement occurred along the fault plane, equivalent to up to 14 m vertically. The concentric faults surround a series of compressional ridges cropping out on the southern flank of vent 3 (Fig. 5a). Nearly half a meter high, these ridges crisscross each other without any consistent orientation; that is they vary from concentric to radial. The F_4 feature has been buried by slumping of unconsolidated tephras in the northern sector of the amphitheatre, preventing the precise temporal relationship with vent 1 to be determined. Nevertheless, the location of F_4 and the compressional ridges at the inner margin of the late stage II lava dome, their insignificant burial, and the fact that they are formed within and offset the stage III tephra indicate that they formed after termination of stage III.

On a broader scale, no large-scale subsidence structures expected during formation of a volumetrically equivalent caldera were identified—even though >9 km³ of magma was erupted from a voluminous magma reservoir at a depth of ~20 km (Schubring 2001). As previously introduced, the basement is highly fractured and appears favorable for the formation of a caldera. For instance, large extensional faults parallel to the Rio Tambo were observed (Lavallée 2003); however, no temporal relationships were established, and therefore their association with subsidence caused by magma removal is purely speculative.

Interpretation of the subsidence structures at Huaynaputina

The various observations presented here enable us to constrain temporally and morphologically the dynamics of local crustal adjustment during the 1600 eruption of Huaynaputina. Furthermore, the observations require a reassessment of some earlier interpretations of vent features introduced by Adams et al (2001). First, the final vestiges of vents 1 and 3 exposes the dike that fed the late stage II lava dome, implying that both vents were formed during stage III; this refines the early idea proposed by

Fig. 5 Features present in the vent area. **a** The *dashed line* indicates the trace of F_1 and the *box* highlights a small fault (F_2) trending 80° in the NE corner of vent 2 (looking N). Two small depressions (*D*) can be seen on each side of the late stage II lava dome. A series of concentric extensional ridges (F_4) surrounds vent 3 and encloses multiple compressional ridges (*C*) on the southern flank of the late stage II lava dome. For scale, the diameter of vent 3 is 280 m; **b** E–W trending fault scarp (F_1) that aligns with a dike in the wall of vent 2 (looking E); **c** Normal fault, parallel with the wall of vent 2, that runs through the E–W trending dike (looking S)
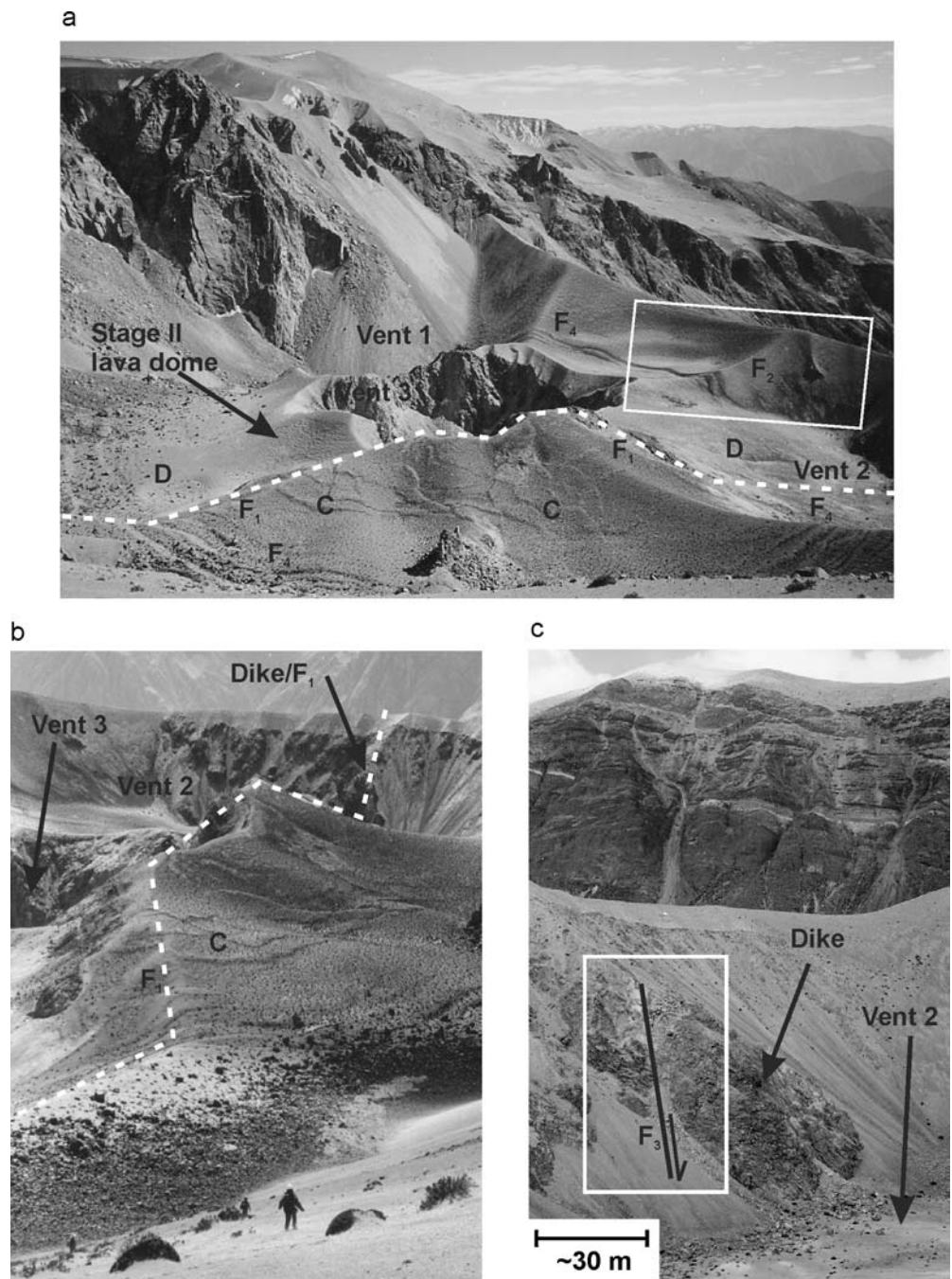
Adams et al. (2001) that the current vent 1 was a remnant of stage I (Fig. 2). Secondly, we showed that vent 2 is outlined by a fault F_3 which, in combination with the faults F_1 and F_2, downfaulted the late stage II lava dome. This observation indicates that the feature named vent 2 by Adams et al. (2001) is not a vent but a subsidence structure that formed mostly after the emplacement of the lava dome. This is one of two subsidence structures described in our survey of the vent area.

The first subsidence structure covers most of the amphitheatre floor and is defined by the faults F_1, F_2, F_3, and the associated series of extensional gashes located beyond the southern amphitheatre rim. The depression, estimated at approximately 0.85 by 0.95 km based on the extent of F_3, results from the collapse of a non-coherent block faulted by the pre-existing E–W trending faults F_1 and F_2. The northern sector is peculiar because it shows the presence of a terrace tilted inwardly by ∼25°. To accommodate for tilting of this crustal block, peripheral extension led to 3 m of displacement along F_3, which developed the length of a pre-existing NW–SE fracture that crosses this area.

Some insights into the formation of the terrace can be gleaned from the observations at Miyakejima volcano, Japan (Geshi et al. 2002). Here, a tilted terrace formed when the collapse dimensions were proportional to that of Huaynaputina (Table 2). After 18 h of subsidence along

Table 2 Parameters of the proximal features used to evaluate their volume. For the volume estimate of the conduit, the depth of the initial vent was subtracted from that of the conduit

Structure	Dimension (m)	Angle (°)	Depth (m)	Area (km^2)	Total volume (km^3)
Initial vent[a]	560×560	30	160	0.25	0.01
Initial vent	560×560	∼75	∼600	0.25	0.08
Cylindrical conduit	250×250		2,400	0.05	0.12
Dyke as a conduit	∼2,000×∼25		2,400	0.05	0.12
Vent 3	280×280	∼75	∼100	0.06	0.002
Dome Subsidence	560×560		14	0.25	0.003
Caldera (northeast)			40	0.05	0.002
Caldera (central)			70	0.55	0.385
Caldera (south)			10	0.05	0.005
Caldera (whole)	850×950		∼70	0.65	0.04
Miyakejima caldera[b]	980×980		120	0.6	0.056

[a]This volume is a minimum estimate based on the assumption that the walls of the vent parallel the steepest concentric extensional fault

[b]These are the dimensions of the caldera at Miyakejima, Japan, as of July 9th 2000 (Geshi et al. 2002)

steep faults, the terrace tilted and slid inward from the over-steepened northwestern wall of the forming caldera (Geshi et al. 2002). This terrace at Miyakejima is identical to the tilted terraces at Huaynaputina, specifically the area between F_2 and F_3, and possibly also similar to the southern area between F_1 and F_3. These features at Huaynaputina therefore likely formed late in the subsidence sequence and in response to subsidence along deep, steep faults.

The main subsidence faults F_1, F_2, and F_3 developed along pre-existing regional faults and are either steeply inward dipping or vertical, an observation which suggests that they penetrate deep into the crust. Crosscutting relationships indicate that faulting initiated during stage II of the eruption. This is consistent with the alternation from pyroclastic falls to flows during this stage (Adams et al. 2001), which we believe was caused by pressure changes as subsidence initiated around the conduit and perhaps into the shallow reservoir. Downfaulting was however mainly active during stage III as indicated by the moderate degree of burial of the faults by erupted tephra and the fact that F_1 and F_2 propagated through the late stage II lava dome. Thus, the temporal relationships suggest that subsidence of the non-coherent collapse structure initiated late when at least 8.8 km^3 of magma had been erupted. Likewise, subsidence at Miyakejima volcano was recognized to have begun 13 days after commencement of magma withdrawal (Kumagai et al. 2001; Geshi et al. 2002). This late onset of subsidence is a common characteristic of small calderas (Yokoyama 1981, 1983; Scott et al. 1996; Lipman 1997; Walter and Troll 2001; Kennedy et al. 2004). Altogether, the steeply dipping faults combined with pre-existing faults to modify the proximal vent area and create a subsidence structure comparable to a non-coherent collapse caldera or a summit pit crater—a small depression resulting from collapse into a reservoir depressurized by magma drainage (see discussion; Roche et al. 2000, 2001). The distinction between the two types of structure is however semantic and beyond the scope of this study. Here, we prefer the term non-coherent collapse which is descriptive of the general morphology.

The second subsidence structure is well defined by a set of concentric extensional faults (F_4) that surrounds multiple crisscrossing ridges (Figs. 3, 5a, 6). The diameter of F_4 is nearly 0.56 km with the outermost fault plane commonly having a dip angle of approximately 30° (Fig. 6c). Extrapolation of the fault planes produces an inverted conical geometry which intersects at a depth of approximately 0.16 km. Analysis of the faults' dip angles shows an outward steepening progression (Fig. 6), suggesting that these normal faults are listric and have rotated each hanging block toward the spoon-shaped fault surface. If true, the inverted conical structure probably does not penetrate as deep as 0.16 km. The F_4 structure and the ridges developed within the late stage II lava dome and were not buried by tephra deposits of stage III, which suggests that they formed after termination of the eruption. The concentric faults and ridges are morphologically similar to those produced during structural resurgence of a caldera (Walter and Troll 2001); however, they are genetically dissimilar. First, the concentric faults are normal in origin rather than reverse and the radial ridges resemble compressed mounds instead of opened fractures. Also, concentric faults accompanying resurgence show an inward steepening progression (Walter and Troll 2001), which is the opposite of what we observe here. Finally, the very shallow depth reached by the listric faults would suggest that magma had been intruded inside the lava dome after stage III without causing an explosion; this we believe is quite unlikely. Similar concentric structures produced by dome subsidence have been described from cycles of dome growth and subsidence at Lascar Volcano, Chile (Matthews et al. 1997) and we believe that F_4 and the ridges at Huaynaputina formed in response to dome subsidence. Even though the displacement along F_4 was only 14 m, it likely caused an inner zone of compression that led to the development of multiple compressional ridges cropping out on the southern flank of vent 3 (Fig. 6). The concentric extensional faults and the compressional ridges are comparable to larger-scale features developed in analogue models of caldera formation (Lavallée et al. 2004). The crosscutting relationships between the concentric extensional faults, the compressional ridges, and the

Fig. 6 Photograph of F_4. **a**–**b** respectively show close up photos of the SW and NE sector of F_4. The faults are highlighted by *tracing lines* and the compressional ridges by *dotted lines*. Both sectors are accompanied by their measured profile located above each photograph. **c** Aerial photo showing the stereonet projections of strike and dip measurements for 11 traverses (*dotted lines*) across F_4. The *two boxes* show the location of the traverses in (a) and (b)
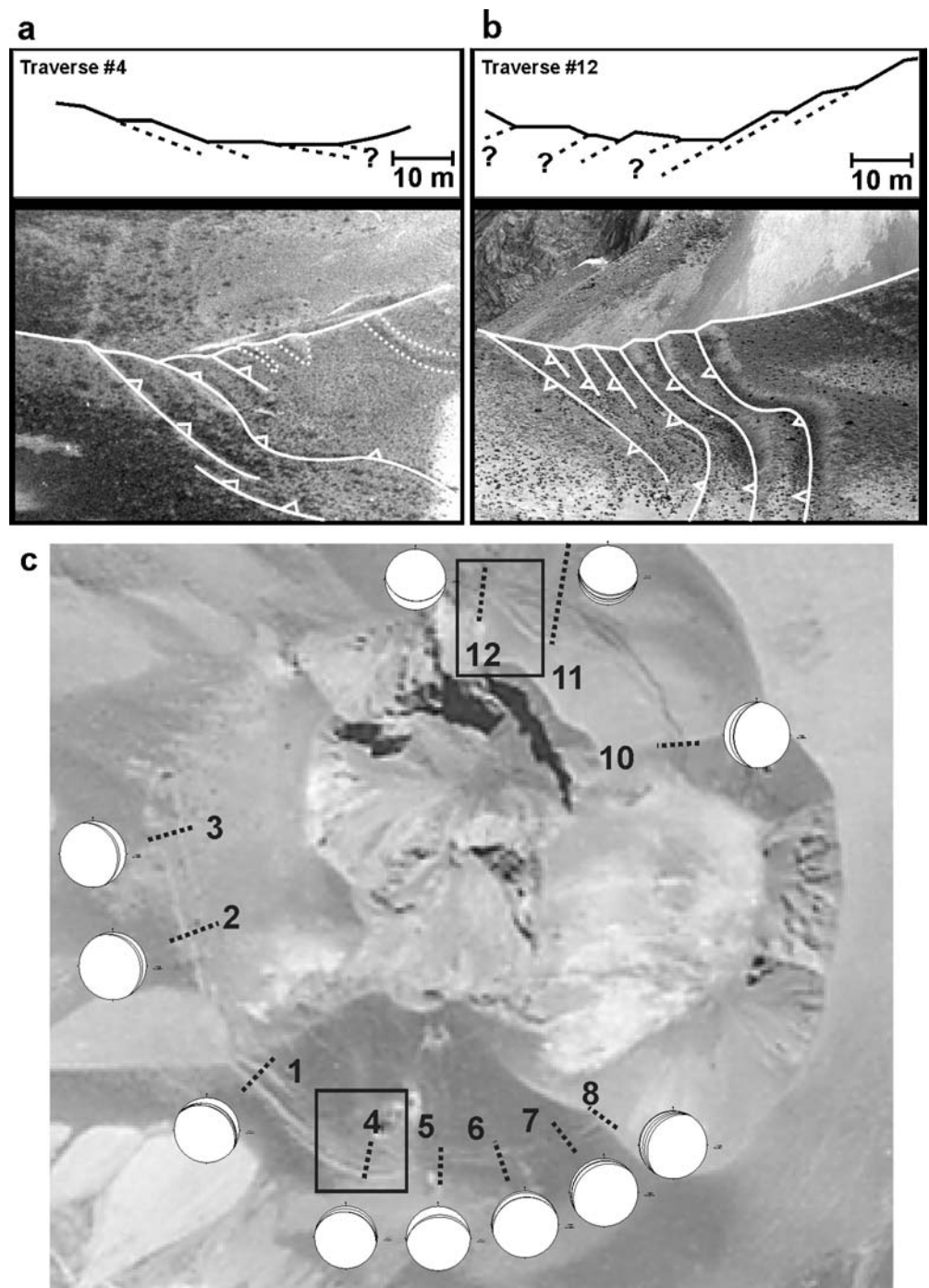
tephra deposits imply that the subsidence structure developed after termination of the eruption by depressurization of the late stage II lava dome and the upper conduit. The second subsidence structure, delineated by F_4, will therefore be referred to as a dome subsidence structure hereafter.

Our work has identified two subsidence features at Huaynaputina: a non-coherent collapse structure superimposed by a dome subsidence structure. While the latter is a minor late stage shallow crustal adjustment, the non-coherent collapse is more substantial. Having established the character of subsidence at Huaynaputina,

we next explore the details of the vents and the extent of collapse to illuminate the underlying cause.

Local fault displacement analysis and volume estimates

Cored-out vent versus lithic content

Understanding the stratigraphy and distribution of exotic lithics in the stage I deposits allows further insight into the conduit and vent forming processes. The lithics in

343

the stage I plinian fall deposits evolve from primarily altered sedimentary rocks from the ~3-km-deep Yura Formation to mainly fresh andesitic lava fragments from the shallower ~1–3-km-deep Matalaque Formation during the latter half of the stage I eruption (Adams et al. 2001). This suggests than the fragmentation level initially must have been at least ~3 km deep (Adams et al. 2001). As the stage I eruption progressed and its intensity rose, the level of fragmentation rose, reaming out the walls in the shallower conduit made of volcanics from the Matalaque Formation. Adams et al. (2001) estimated that the volume of exotic lithics reamed out during stage I was 0.18 km^3. This is an approximate minimum estimate for the size of the cored-out vent and conduit.

The vent that was cored out during the stage I plinian eruption can only be as large as the vent in which the lava dome was emplaced at the end of stage II. For calculation purposes, it is assumed here that the maximum diameter of the initial vent was that of the lava dome outlined by F$_4$ which is 0.56 m. The depth of the vent is difficult to estimate, but assuming the slope of the vent wall was similar to those of vent 1 and 3, with an angle of ~75°, the depth and volume of the initial vent were evaluated to be ~0.6 km and 0.08 km^3, respectively (Table 2). This volume deficit compared with the lithic estimate of 0.18 km^3 is significant. We suggest that the remaining portion of lithics is derived from below the cored-out vent through entrainment of wall rock along the conduit connecting the shallow reservoir to the surface. Based on petrological studies, Schubring (2001) proposed the shallow magma reservoir roof at a depth of ~4 km and Adams et al. (2001) proposed the initial fragmentation level at >3 km. If we conservatively assume that lithics were only excavated from a cylindrical conduit extending from the fragmentation level at 3 km to the bottom of the vent at 0.6 km, the conduit diameter would be approximately 0.25 km (Table 2); this simplistic approach yields a large value nearly equal to the diameter of vent 3, which we believe is unlikely. Two fractures were present prior to the 1600 eruption of Huaynaputina: one NW–SE and one E–W. The magma most probably intruded upward through one or both of these fractures. This is consistent with the late occurrence of an explosion at vent 4 located nearly 2 km south of the main vent. The morphology of such an elongated dike cannot be accurately estimated, but assuming a length of 2 km and a vertical extent of 2.4 km, the width of the conduit would be on the order of 20–30 m, which is a more realistic dimension (Table 2).

Magma erupted versus subsidence structures

To appreciate the extent of subsidence at Huaynaputina, we calculated the volume of both subsidence structures and compared them with the current estimates of eruptive volumes which were recently refined by Adams et al. (2001). Thickness measurements coupled with laboratory determination of ash and pumice densities demonstrate that the initial stage withdrew at least 8.8 km^3 DRE from the magma chamber. The second and third stages, which are more lo-cally distributed and volumetrically smaller, erupted about 1 km^3 DRE each.

The non-coherent collapse structure covers an area of ~0.65 km^2 and shows a variable amount of displacement (Table 2). Using the values of subsidence and the area of each of the sectors, the volume of the structure was estimated at a minimum of 0.04 km^3 (Table 2). We previously established that subsidence occurred during stages II and III meaning that a maximum of 2 km^3 of magma erupted from the shallow reservoir and the conduit while the 0.04 km^3 collapse structure formed. The formation of extensional gashes located 1.5 km south of the collapse structure indicates that some of the underpressure derived from the NW–SE dike-shape conduit. The possibility that the subsidence was caused only by the depressurization of the dike is unlikely based on a comparison of the dimensions of these features. The non-coherent collapse structure subsided along a steeply dipping ring fault with dimensions of 0.85 by 0.95 km while the dike is only 20–30 m wide. Additionally, subsidence of the collapse structure can only have resulted from the removal of magma present directly underneath it. The 0.12-km^3 dike-shape conduit extends beyond the limit of the collapse structure and here we argue that the volume of the dike beneath the 0.95-km-wide collapse structure was half of its full volume and therefore ~0.06 km^3. This volume is comparable to that of the collapse structure, which would imply that all the magma present in the portion of the dike beneath the collapse structure was drained to allow this amount of subsidence. These volume comparisons allow us to speculate that underpressure in the dike alone was not sufficient enough to achieve the non-coherent collapse structure and therefore the evacuation of the shallow magma reservoir likely contributed to the underpressure.

Using fault displacements measured in situ, vertical subsidence of the dome along F$_4$ averages 14 m. The circular structure covers a diameter of 0.56 km and thus the total volume of the dome subsidence structure is only 0.003 km^3 (Table 2). When extrapolated, the listric faults reach a maximum depth of 0.16 km, which is nearly the depth of the exposed portion of vent 3. Withdrawal of lava from the conduit beneath the eviscerated vent at the end of stage III may have caused the underpressure which caused subsidence of the dome. It is also possible that a late-stage dome phenomenon such as degassing caused the pressure changes responsible for the dome subsidence.

Together, the volume estimates of the two subsidence structures total ~0.043 km^3. This is 0.4% of the total magma volume erupted (Adams et al. 2001). Schubring (2001) proposed that the 9 km^3 of magma erupted during stage I originated from a depth of 20 km, while the 2 km^3 of the later two stages were entrained from a shallow reservoir. Crosscutting relationships in the vent area indicate that both subsidence structures were formed rather late in the eruptive sequence. Their formation probably coincided with the drainage of the shallow reservoir and the conduit, but this is open to debate. What is clear, however, is that these subsidence structures did not counterbalance the volume of magma erupted.

Subsidence in the temporal framework of the eruption

Our work presented here, coupled with petrological analysis (Schubring 2001) and earthquake data (Ceresis 1985), allow us to refine the vent evolution briefly introduced by Adams and others (2001). The eruption was preceded by earthquakes near the shallow magma reservoir at a depth of 6 km and around a depth of 20 km (Fig. 1; Ceresis 1985), which is consistent with the ascent of the stage I magma from the deep reservoir (Schubring 2001). Onset of the eruption on February 19 was characterized by an increase in intensity of shallow and deep earthquakes (Ceresis 1985; de Silva et al. 2000). Fragmentation initiated within the Yura Formation at a depth greater than 3 km (Adams et al. 2001). The morphological character of the vent area suggests that the first vent developed along the NW–SE fracture and at the intersection with a E–W fault (Fig. 7a). The steady evolution of the intensity (increase then decrease) of the stage I eruption, albeit with short periods of vent clearing, suggests that coring out of the vent took place during this stage (Fig. 7b; Barriga 1951; Ceresis 1985; Adams et al. 2001).

After nearly 4 days of quiescence, stage II of the eruption ensued with magma originating from the shallow reservoir at depths of 4–6 km (Schubring 2001). Subsidence along F_1 initiated during stage II (Fig. 7c). Subsidence would have altered the size of the vent, causing eruption column instability and the generation of pyroclastic flows, which are common stage II deposits. Furthermore, intense earthquakes were felt by the nearby population during this stage (de Silva et al. 2000). At the end of stage II, the eruptive style changed and a lava dome was emplaced within the cored-out vent (Fig. 7d).

After nearly 2 days of quiescence during which pressure built up in the dome, a vulcanian eruption eviscerated the dome and produced vent 3 (Fig. 7e and 8a). Initiation of stage III was accompanied with renewal of strong earthquakes at depth (de Silva et al. 2000). As the eruption progressed, the shallow magma reservoir and the conduit further depressurized, removing the support to the overlying crust, and subsidence continued along F_1 in conjunction with F_2 and F_3 (Fig. 7f and 8b). Subsidence along steep faults at depth caused limited peripheral extension and inward tilting of terraces in the north and the south (Fig. 8b). Accompanied depressurization of the dike exerted further tension to the surrounding areas and peripheral extensional gashes began to develop on the southern flank of the amphitheatre (Fig. 7f). As stage III of the eruption waned, vent

Fig. 7 Sketch showing a 9-stage evolution of the vents and structures during the eruption: **a** vent 1 formation along the NW–SE fissure; **b** vent 1 enlargement into vent 2; **c** possible subsidence initiation along F_1 and continued coring out of the initial vent; **d** dome emplacement within the central, cored-out vent; **e** evisceration of the dome, forming vent 3; **f** (re)initiation of subsidence along F_1 in conjunction with F_2, F_3 and the tensional gashes; **g** re-opening of vent 1 in the NW portion of the central dome; **h** termination of the eruption and subsidence along a set of extensional faults concentric to vent 3, which produced inner compressional ridges; and **i** excavation of vent 4 during a final explosion and formation of two small depressions at the base of F_1
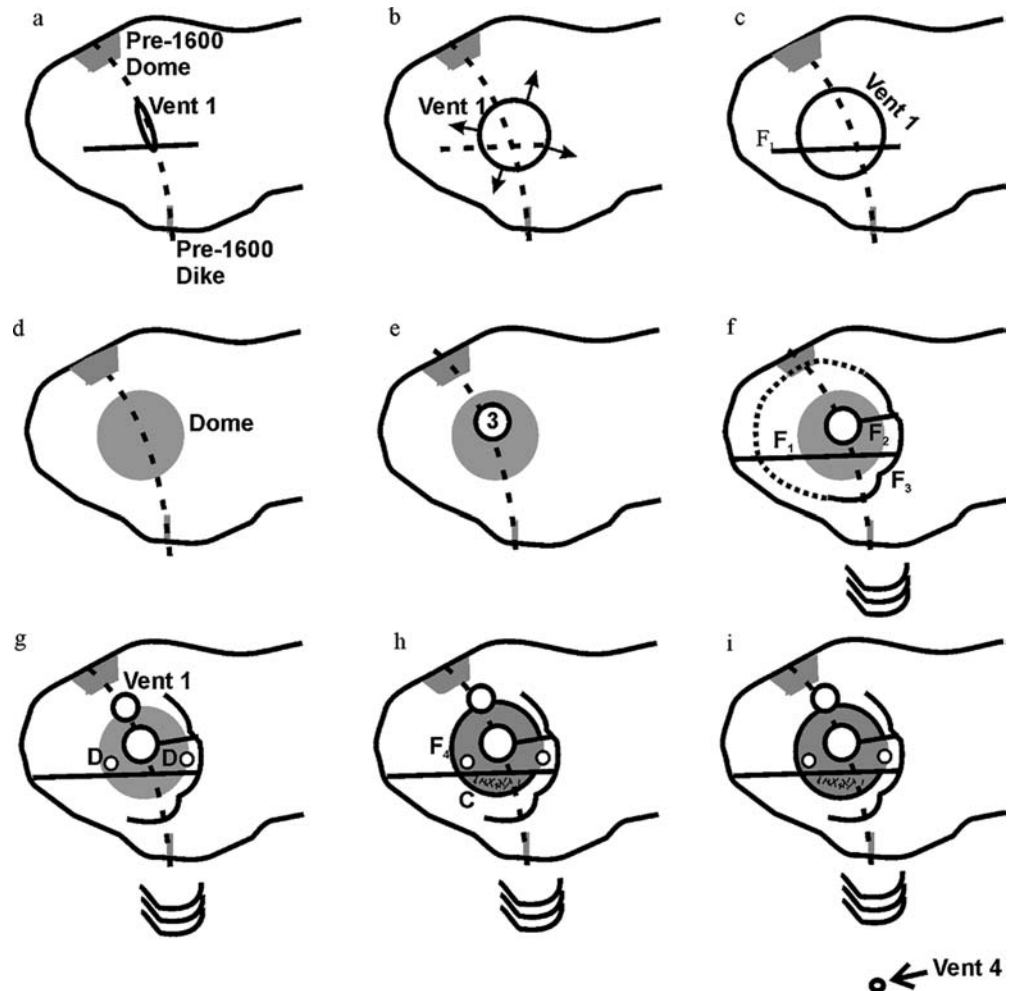
Fig. 8 Cross sectional sketch of Huaynaputina, showing the evolution of the proximal subsidence structures during stage 3 (**a–c**) and the relationship between the deep and the shallow magma chambers (**d**). **a** evisceration of the late-stage II dome forming vent 3; (**b**) subsidence along F_1, F_2, and F_3 (E formed in periphery are not shown here); (**c**) subsidence along F_4 and formation of the compressional ridges. The *black vertical line* shows the E–W dike crossing the vent area. No vertical exaggeration; (**d**) Large-scale cross-section beneath Huaynaputina, where faults connect the shallow and deep magma chambers to the surface. The shallow magma chamber is thought to have reopened by minor re-adjustment of underlying crustal blocks into the deep chamber. The *light gray* represents the stage I magma, the *medium gray* represents the mixed stage II magma, and the *dark gray* represents the crystal mush erupted in stage III
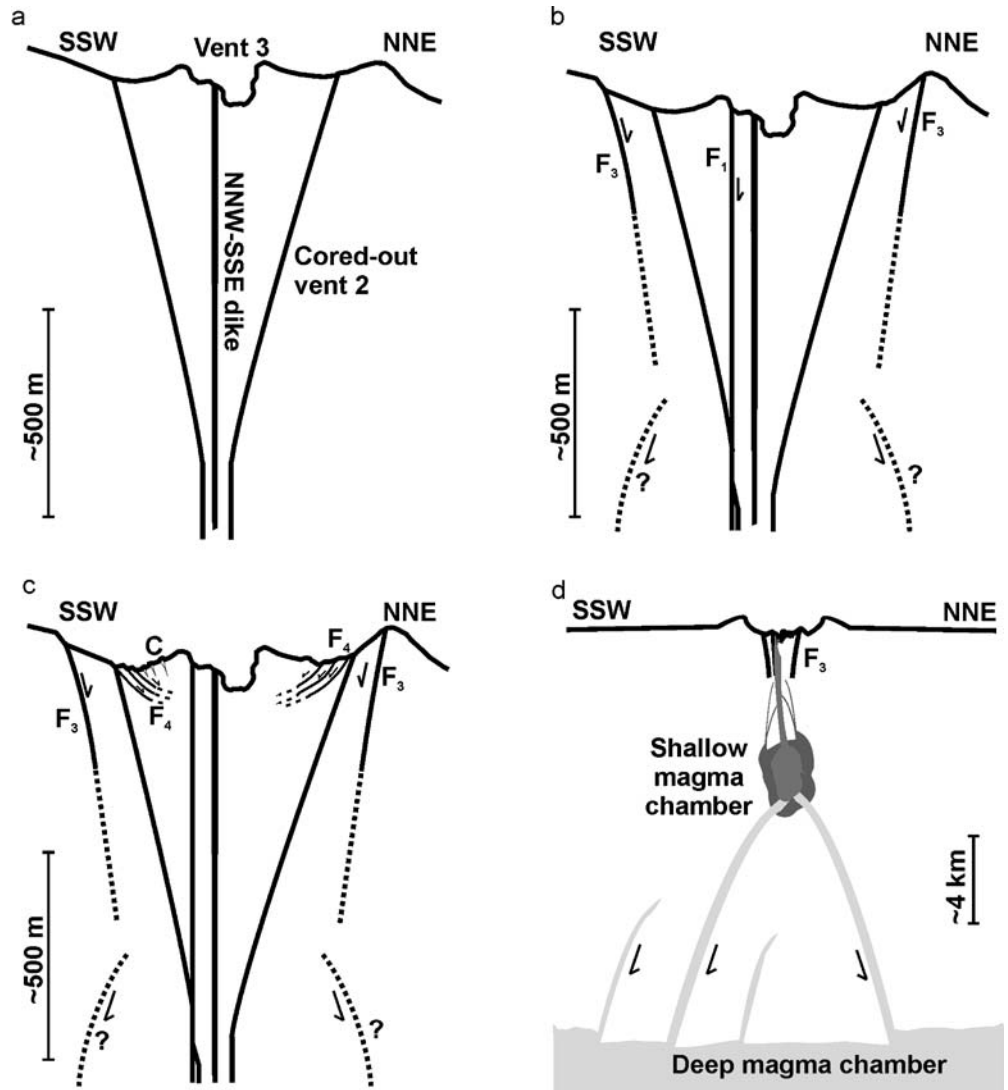
1 was briefly re-initiated through the NW margin of the dome (Fig. 7g). Subsidence along F_2 terminated, but along F_1 subsidence continued in certain areas causing the formation of two small depressions at the base of F_1 (Fig. 7g). The shallow pressure release associated with cessation of magma ascent through the main conduit then led to the late formation of F_4 and compressional ridges (Fig. 7h and 8c). A final explosion occurred along the NW–SE dike-shape conduit on the southern flank of the amphitheatre, creating vent 4 (Fig. 7i).

The subsidence structures observed at Volcán Huaynaputina are restricted to the vent area. The evolution of these proximal structures was the result of coring out, depressurization, non-coherent collapse, and dome emplacement, followed by renewed collapse of the non-coherent structure and subsidence of the dome. While it is clear that the pressure variations that contributed to the collapses would not have been possible without the presence of a shallow magma reservoir and a dike, our interpretation of the non-coherent collapse structure does not allow us to ascertain the origin of the underpressure that led to subsidence. More-over, while this analysis helps us better understand the nature of subsidence and the possible causes, the issue of why no major collapse is associated with this eruption remains.

Discussion: cryptic or non-collapse at sites of major explosive eruptions

A significant number of recent explosive eruptions have no volumetrically equivalent caldera collapse at the eruption site. Volcanoes Quizapu, Cerro Hudson, and Lascar in Chile, Santa María in Guatemala, and Novarupta in Alaska are good analogies to Huaynaputina (Hildreth and Drake 1992; Scasso et al. 1994; Gardeweg et al. 1998; Williams and Self 1983; Wallman et al. 1990 respectively). Non- or cryptic collapse may be far more common than we realize as these celebrated examples are youthful and in most cases were either observed or have well-preserved tephra deposits that telegraph the explosive eruption. Older examples where ephemeral tephra deposits are lost from the record might not be identified.

The absence of equivalent collapse at the eruption site of various volcanic systems with large explosive eruptions remains enigmatic. Contributing factors identified include the depth and geometry of the magma body (e.g., Santa María, Cerro Hudson, and Lascar; Williams and Self 1983; Scasso et al. 1994; Gardeweg et al. 1998 respectively), and its complex subsurface connectivity or its size (e.g., Novarupta and Quizapu; Wallman et al. 1990; Hildreth and Drake 1992). All of these factors ultimately affect the magnitude of underpressure that allows subsurface crustal adjustment, inhibiting the development of a single equivalent caldera. We believe that this is consistent with what we can glean from Huaynaputina.

Insights from Huaynaputina

Subsurface evolution of the magmatic and structural activity at Huaynaputina can be reconciled through integration of petrological evidence (Schubring 2001) and seismic data compiled by the SISRA project (Ceresis 1985). Silicic-silicic magma interaction has been identified at Huaynaputina (Schubring 2001); a hotter, less-evolved dacite (Dacite 1) punched through a pre-existing mush of cooler more evolved dacite (Dacite 2) to initiate the 1600 eruption. Dacite 1 is interpreted as the product of differentiation of an andesitic magma batch that was rising from a deep reservoir. Dacite 2 is constrained as a crystal mush which was ponding between $\sim$6 km (amphibole geobarometry) and $\sim$4 km (residual glass chemistry). Dacite 1 erupted during stage I, while mingled products of Dacite 1 and 2 and pure Dacite 2 erupted during stages II and III. Thus on the basis of petrology, two magma bodies have been inferred beneath Huaynaputina: a deep one around a depth of 20 km (the UHTS), and a shallow one between 4 and 6 km (Schubring 2001).

The coordinates and depth of earthquakes that occurred in 1600 were estimated by the SISRA project via historical accounts (Fig. 1; Ceresis 1985) These data indicate earthquakes at about 20 and 6 km throughout the eruption at Huaynaputina. Notwithstanding that the accuracy of the depth of the data for such old events is relatively poor, it is interesting that the earthquake data correlates to the petrological results (Schubring 2001) and our structural observations. These two lines of evidence combined with our interpretation of the physical evolution of the vent region given above suggest the following interpretation. As a large batch of andesite (>9 km^3) ascended from the deep reservoir (the UHTS, >25 km) along the arcuate NW–SE fracture and the E–W fault, crustal blocks above the UHTS likely subsided to compensate for the volume deficit. While subsidence occurred at depth, dilatation of deep faults and intersection of the faults at depth prevented broad subsidence from occurring at the surface (e.g., Roche et al. 2001; Acocella et al. 2000; Walter and Troll 2001). This restricted subsidence may have caused enlargement of the shallow reservoir (Fig. 8d) which permitted Dacite 1 magma to fill in and partially mix with the residual crystal mush that had formed the pre-1600 dikes and domes.

A review of the literature on caldera formation shows that crustal subsidence above a deep magma chamber may generate faults which intersect at depth and form cavities (e.g., Miyakejima, Japan; Furuya et al. 2001; Geshi et al. 2002; Fig. 8d). Experimental studies also demonstrate that for magma reservoirs with roof aspect ratios (i.e., thickness-to-width ratio of the magma chamber's roof) greater than about 1.4, subsidence-controlling faults will intersect at depth before reaching the surface (Fig. 8d; Roche et al. 2000; Roche and Druitt 2001). This fault geometry leads to an unstable upper roof which subsides incoherently. The subsidence caused by depressurization of a deep chamber is significantly smaller than the evacuated volume (Kennedy 2000). This relationship is caused by dilatation of subsidence-controlling faults, which induce an expansion of the subsiding roof, minimizing the surface expression. In more extreme examples where the roof aspect ratio exceeds 1.4, the subsidence controlling faults may intersect at depth and stop propagating upward. If the roof is stable, a cavity is created at depth, and underground collapse may cause the roof to sag (Branney 1995; Troll et al 2000). These processes may explain the absence of a volumetrically equivalent caldera at the site of large explosive eruptions. At Huaynaputina, the occurrence of earthquakes at $\sim$6 and $\sim$20 km in the year 1600 attests to structural activity at these depths, and conceivably to the adjustment of the country rocks during the eruption.

We can use petrological data and our structural analysis to constrain the dimensions of the shallow magma reservoir. During stages II and III, approximately 2 km^3 of magma was evacuated from the shallow reservoir located between approximately 4 and 6 km (Schubring 2001; Adams et al. 2001). These depth range and volume data yield a cylindrical reservoir with a diameter of 1.3 km. The roof aspect ratio of a 1.3-km-wide magma reservoir located at a depth of 4 km is 3 and upon its complete evacuation the development of a small caldera with non-coherent floor is favored (Roche and Druitt 2001). Schubring (2001) suggested that the eruption at Huaynaputina drained the crystal mush present in the shallow reservoir and we observed that the small collapse structure developed at Volcán Huaynaputina has a non-coherent floor. The collapse structure subsided along steeply dipping to vertical faults and has an approximate diameter of 0.85 by 0.95 km, which is comparable to the estimated diameter of the shallow reservoir. We suggest that the extensive magma withdrawal from the shallow reservoir enabled subsidence at a late stage in the eruption sequence. Huaynaputina shows the early configuration of a non-coherent collapse due to depressurization of the conduit and the shallow magma reservoir.

Reference

Acocella V, Cifelli F, Funiciello R (2000) Analogue models of collapse calderas and resurgent domes. J Volcanol Geotherm Res 104:81–96

Adams NK, de Silva SL, Self S, Salas G, Schubring S, Permenter JL, Arbesman K (2001) The physical volcanology of the 1600 eruption of Huaynaputina, southern Peru. Bull Volcanol 62:493–518

Barriga VM (1951) Los Terremostos en Arequipa (1582-1868). La Colmena, Arequipa

Branney MJ (1995) Downsag and extension at calderas: new perspectives on collapse geometries from ice-melt, mining and volcanic subsidence. Bull Volcanol 57:303–318

Branney MJ, Kokelaar P (1994) Volcanotectonic faulting, soft-state deformation, and rheomorphism of tuffs during development of a piecemeal caldera, English Lake District. Geol Soc Am Bull 106:507–530

Carrasco Viza R (2002) Caracteristicas petrographicas y geo-quimicas del grupo Barroso en los cuandrantes III y IV del quadrangulo de Ichuna (33–u). Thesis, Universidad National San Agustin de Arequipa, Peru, pp 1–108

Ceresis (1985) Catalogue of earthquakes for South America: description of the catalog and national reports. In: AskewBL, AlgermissenST (eds) Asociación de Publicaciones Educativas, Lima, Peru, pp 1–191

de Silva SL, Francis PW (1990) Potentially active volcanoes of Peru: observations using Landsat Thematic Mapper and space shuttle photography. Bull Volcanol 52:286–301

de Silva SL, Alzueta J, Salas G (2000) The socioeconomic consequences of the 1600 AD eruption of Huaynaputina, southern Peru. In: McCoy F, Heiken G (eds) Volcanic disasters in human antiquity. Geol Soc Am Spec Pap 345

Druitt TH, Sparks RSJ (1984) On the formation of calderas during ignimbrite eruptions. Nature 310:679–681

Fenner CN (1921) The Katmai region, Alaska, and the great eruption of 1912. J Geol 28:569–606

Folch A, Marti J (2004) Geometrical and mechanical constraints on the formation of ring-fault calderas. Earth Planet Sci Lett 30:215–225

Fouqué F (1879) Santorin et ses éruptions. Masson, Paris, pp 1–440

Furuya M, Okubo S, Yamamoto E, Okada Y, Kikuchi M (2001) Volcanic earthquakes and tremors associated with the 2000 Miyakejima volcanic eruption (in Japanese with English Abstract). J Geogr 156:191–203

Gardeweg MC, Sparks RSJ, Matthews SJ (1998) Evolution of Lascar volcano, northern Chile. J Geol Soc London 155:89–104

Geshi N, Shimano T, Chiba T, Nakada S (2002) Caldera collapse during the 2000 eruption of Miyakejima Volcano, Japan. Bull Volcanol 64:55–68

Hildreth W, Drake RE (1992) Volcán Quizapu, Chilean Andes. Bull Volcanol 54:93–125

Hildreth W, Fierstein J (2000) Katmai volcanic cluster and the great eruption 1912. Geol Soc Am Bull 112:1594–1620

INGEMMET (2000a) Mapa geologico del cuadrangulo de Omate (34-u); escala 1:5000. Instituto Geologico Minero y Mitalurgico, Lima, Peru

INGEMMET (2000b) Mapa geologico del cuadrangulo de Ichuna (33-u); escala 1:5000. Instituto Geologico Minero y Mitalurgico, Lima, Peru

James DE, Brooks C, Cuyubamba A, (1976) Andean Cenozoic volcanism: magma genesis in the light of strontium isotopic composition and trace element geochemistry. Geol Soc Am Bull 87:592–600

Kennedy B (2000) The nature and origin of caldera structure and morphology, using results from analogue modeling. MSc Thesis, McGill University, Montreal, Canada, pp 131

Kennedy B, Stix J, Vallance JW, Lavallée Y, Longpre M-A (2004) Controls on caldera structures: results from analogue sandbox modeling. Geol Soc Am Bull 116:515–524

Kumagai H, Ohminato T, Nakano M, Ooi M, Kubo A, Inoue H, Oikawa J (2001) Very-long-period seismic signals and caldera formation at Miyake Island, Japan. Science 293:687–690

Lavallée Y (2003) Constraining funnel caldera processes at Volcán Huaynaputina, southern Peru. MSc Thesis, University of North Dakota, Grand Forks, North Dakota, pp 112

Lavallée Y, Stix J, Kennedy B, Richer M, Longpre M-A (2004) Caldera subsidence in areas of variable topographic relief: results from analogue modeling. J Volcanol Geotherm Res 129:219–236

Lipman PW (1984) The roots of ash flow calderas in the western North America: windows into the tops of granitic batholiths. J Geophys Res 89:8801–8841

Lipman PW (1997) Subsidence of ash-flow calderas: relation to caldera size and magma-chamber geometry. Bull Volcanol 59:198–218

Matthews SJ, Gardeweg MC, Sparks RSJ (1997) The 1984 and 1996 cyclic activity of Lascar Volcano, northern Chile: cycles of dome growth, dome subsidence, degassing and explosive eruptions. Bull Volcanol 59:72–82

Mendívil S (1963) Geologia de tierras en el distrito de Ubinas. Com Carta Geol Nac Bol 13

Mercier JL, Sebrier M, Lavenu A, Cabrera J, Bellier O, Dumont J-F, Machare J (1992) Changes in the tectonic regime above a sub-duction zone of Andean type: the Andes of Peru and Bolivia during the Pliocene-Pleistocene. J Geophys Res 97:11945–11982

Moore I, Kokelaar O, (1998) Tectonically controlled piecemeal caldera collapse: a case study of Glencoe volcano, Scotland. Geol Soc Am Bull 110:1448–1466

Roche O, Druitt TH (2001) Onset of caldera collapse during ignimbrite eruptions. Earth Planet Sci Lett 191:91–202

Roche O, Druitt TH, Merle O (2000) Experimental study of caldera formation. J Geophys Res 105:395–416

Roche O, van Wyk de Vries B, Druitt TH (2001) Sub-surface structures and collapse mechanisms of summit pit craters. J Volcanol Geotherm Res 105:1–18

Scandone R (1990) Chaotic collapse of calderas. J Volcanol Geotherm Res 42:285–302

Scasso RA, Corbella H, Tiberi P, (1994) Sedimentological analysis of the tephra from the 12–15 August 1991 eruption of Hudson volcano. Bull Volcanol 56:121–132

Schubring S (2001) The petrology and geochemistry of Volcan Huaynaputina, southern Peru. MSc Thesis, Indiana State University, Terre Haute, Indiana 35

Scott WE, Hoblitt RP, Torres RC, Self S, Martinez M, Nillos Jr. T (1996) Pyroclastic flows of the June 15, 1991 climactic eruption of Mount Pinatubo. In Newhall CG, Punongbayan RS (eds) Fire and mud: eruptions and lahars of Mount Pinatubo, Philippines. University of Washington Press, Seattle, Washington, pp 545–570

Smith RB, Bailey RA, (1968) Resurgent cauldrons, Geol Soc Am Mem 116:83–104

Thouret J-C, Juvigne E, Gourgaud A, Boivin P, Davila J (2002) Reconstruction of the AD 1600 Huaynaputina eruption based on the correlation of geologic evidence with early Spanish chronicles. J Volcanol Geotherm Res 115:529–570

Tosdal RM, Farrar E, Clark AH (1981) K-Ar geochronology of the Late Cenozoic volcanic rocks of the cordillera occidental, southernmost Peru. J Volcanol Geotherm Res 10:157–173

Troll VR, Emeleus CH, Donaldson CH (2000) Caldera formation in the Rum central igneous complex, Scotland. Bull Volcanol 62:301–317

Vicente J-C (1989) Early Late Cretaceous overthrusting in the western cordillera of southern Peru. In: Ericksen GE, Canas MT, Reinemun JA (eds) Geology of the Andes and its relation to hydrocarbon and mineral resources: Houston, Texas, 11:91–117

Walker GPL (1984) Downsag calderas, ring faults, caldera sizes, and incremental calderas growth. J Geophys Res 89:8407–8416

Wallman PC, Pollard DD, Hildreth W, Eichelberger JC (1990) New structural limits on magma chamber locations at the Valley of Ten Thousands Smokes, Katmai National Park, Alaska, Geology 18:1240–1243

Walter TR, Troll VR (2001) Formation of caldera periphery faults: an experimental study. Bull Volcanol 63:191–203

Williams H (1941) Calderas and their origin. Univ Calif Dept Geol Sci Bull 25:239–346

Williams H, McBirney AR (1979) Volcanology. Freeman, San Francisco

Williams SN, Self S (1983) The October 1902 plinian eruption of Santa Maria Volcano, Guatemala. J Volcanol Geotherm Res 16:33–56

Yokoyama I (1981) A geophysical interpretation of the 1883 Krakatau eruption. J Geophys Res 9:359–378

Yokoyama I (1983) Gravimetric studies and drilling results at the four calderas in Japan. In: Shimozuru D, Yokoysms I (eds) Arc volcanism: physics and tectonics. Terra, Tokyo, 29–41